Novel Image processing to restore scattered light-sheet microscopic imaging technique and its application for quantifying biomechanics

Tanveer Teranikar¹, Phuc Nguyen¹, Juhyun Lee^{1,2}

¹Joint Department of Bioengineering, University of Texas at Arlington, UT Southwestern Medical Center.

² Department of Medical Education, Texas Christian University

List of abbreviations.

Light-sheet fluorescence microscopy (LSFM) region of interest (ROI) dark channel prior (DCP) field of view (FOV) point spread function (PSF) selective plane illumination microscopy (SPIM) difference of Gaussian (DoG) human visual perception (HVP) hours post fertilization (hpf) Hessian difference of Gaussian (HDoG)

ABSTRACT

Research of cellular and molecular processes by way of histological methods allows for some insight, but comes with a fundamental set of constraints that are challenging to overcome. Traditional histological methods are laborious, as well as severely limiting for in-depth study of developmental processes or disease processes in vivo. In traditional histology, fixing and sectioning tissue necessarily eliminates its dynamic function, while tissue section thickness limits the scope of investigation with conventional imaging tools. Noninvasive in vivo study of tissues and biomarkers is therefore paramount in gaining a fuller understanding of the pathophysiology surrounding conditions like congenital heart disorders. Light-sheet fluorescence microscopy (LSFM) is a powerful and noninvasive optical microscopy tool that can image in vivo tissue function in 4D (3D + time). LSFM boasts benefits such as short pixel dwell time and therefore minimal photobleaching) while maintaining the ability to image a high dynamic range, as well as deep-tissue optical sectioning. Researchers have been seeking to overcome this problem by developing tissue clearing techniques to attempt to homogenize the refractive index across the tissue via removal of light-scattering pigments and lipids. Even so, anisotropy and light scatter are pervasive effects stemming from tissue thickness and refractive index mismatching of mounting media, making optical sectioning with perfectly tuned acquisition parameters difficult to achieve. Therefore, pre- and post-processing techniques are critical for yielding images suitable for biomedical research. Two such novel techniques are presented here.

Keywords: Light-sheet microscopy, Segmentation, dynamic cell tracking

CORRECTING ANISOTROPIC INTENSITY IN LIGHT SHEET IMAGES USING DEHAZING AND IMAGE MORPHOLOGY

In biomedical research, there has long been a demand for specimen images that are free of aberrations in the region of interest (ROI)⁷. However, in LSFM, unfocused fluorescence in the axial direction while scanning deeper into tissue creates a challenge in distinguishing foreground from background⁷. Additionally, light scatter due to refractive index heterogeneity throughout the tissue and in the mounting medium¹⁰ results in axial and lateral blurriness¹¹, making isotropic resolution of volumetric reconstruction challenging, especially in high density tissue samples.

To correct anisotropic intensity in a raw image [Figs. 1(a), 1(c), 2(a), 3(b), 3(e), and 4(a)], the dark channel prior (DCP) illumination correction algorithm was used in conjunction with a background subtraction method. First, dehazing was performed with the DCP algorithm, which was used under the assumption that light is traveling underwater rather than through air¹²⁻¹⁵ and is highly sensitive to noise while correcting medium-dependent attenuation along the line of sight¹⁶. Dehazing takes atmospheric light and transmission distance into account, resulting in restoration of object radiance at zero viewing distance without loss of information or addition of noise⁷ [Fig. 3(c)].

The DCP algorithm also tends to restore autofluorescence experiencing forward scatter [Figs. 1(e) and 3(c)], so background subtraction with a rolling ball averaging algorithm is used to eliminate the scatter⁷ [Figs. 1(b), 1(d), 2(b), 2(d), and 3(d)]. The background subtraction isolates fluorescence-tagged structures in the field of view (FOV) and subtracts out-of-focus objects⁷.

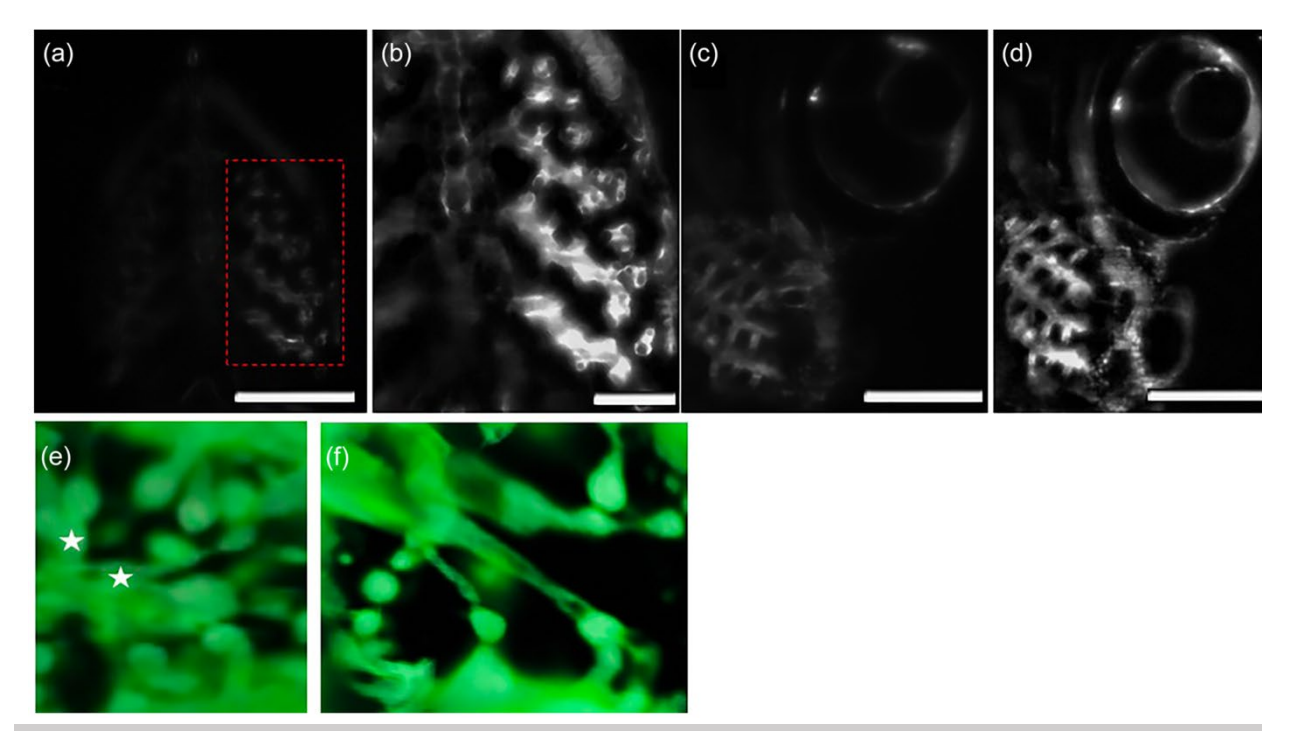


Figure 1^7 . Achieving uniform intensity of zebrafish cranial vasculature with a combination of dehazing and background subtraction. (a) Raw image acquired with oblique scanning superresolution stage on a light sheet fluorescence microscope. Scale bar: $200 \, \mu m$. (b) Magnified view of ROI in red box from (a). Intensity was restored by dehazing to fix attenuation, and background subtracting to remove diffuse light. Scale bar: $100 \, \mu m$. (c) Raw image acquired using the same methods as (a). Scale bar: $200 \, \mu m$. (d) Intensity-corrected version of (c). Scale bar: $200 \, \mu m$. (e) Z-stack images acquired using light sheet fluorescence microscope with dual-sided illumination. White stars: poor separation of objects results in indistinguishable local morphology. This is due to light scatter in the FOV due to refractive index mismatch, which saturates the ROI and yields poorly delineated overlapping structures. (f) Processed 3D image. Intensity is uniform and edges of overlapping objects in the z-stack are enhanced, resulting in spatial integrity in the 3D image.

Anisotropy of the fluorescent bead in manifests as skew in the axial and lateral resolution point spread function (PSF) graphs⁷. After dehazing by DCP, axial and lateral resolution improvements were seen in the PSF⁷. Random noise introduced by deconvolution was then eliminated with an edge preserving bilateral smoothening filter⁷. Performing deconvolution on background subtracted images using dehazed PSF has shown to be a promising method for symmetric restoration of objects in the focal plane⁷ [Figs. 2(c), 2(e), and 3(e)].

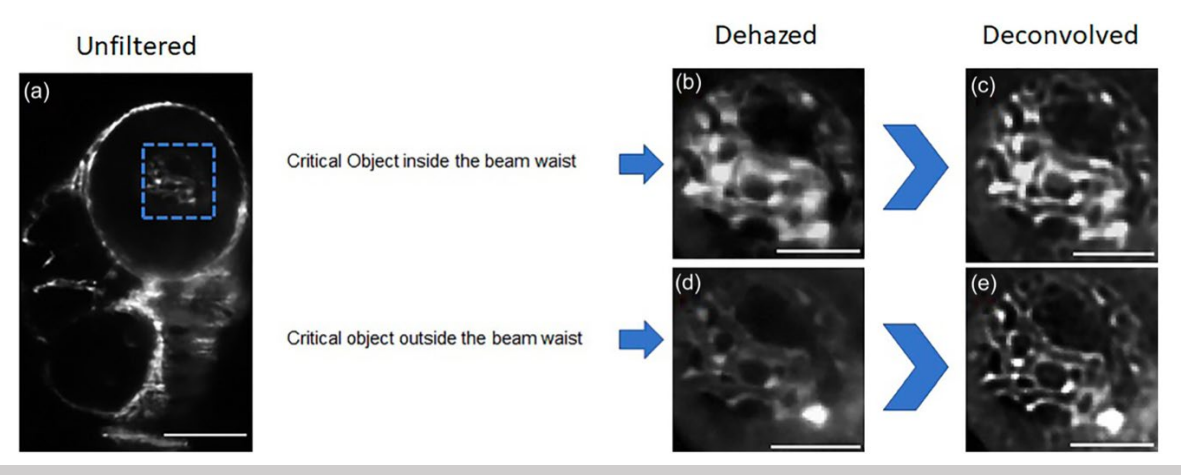


Figure 2⁷. Dehazing and deconvolution. (a) Raw image acquired with light sheet fluorescence microscope using oblique scanning super-resolution stage. Scale bar: 200 μm. (b) Magnification of blue box ROI from image (a). Image is background subtracted and dehazed. Scale bar: 100 μm. (c) Blurred overlapping depth structures in image (b), due to axial gradient refractive index, are now visible after deconvolution. Scale bar: 100 μm. (d) The same procedure is performed on an attenuated image with the light sheet passing through the critical object to compare against saturated image (b) where the light sheet is perpendicular to the critical object. Scale bar: 100 μm. (e) Contour in the ROI is defined after deconvolution. An edge preserving bilateral smoothening filter is applied to images (c) and (e) to remove noise introduced by deconvolution. Scale bar: 100 μm.

Next, a top-hat morphological transform was used to 1) remove vague connections between ROI leftover from the background subtraction step, and 2) further resolve image boundaries⁷. Finally, a bottom-hat transform improves blurred depth details caused by autofluorescence impacts to the axial resolution⁷.

This method was successfully applied to images acquired with various LSFM modalities including single/dual selective plane illumination microscopy (SPIM), multiview SPIM with dual illumination, and the voxel super-resolution technique using an oblique scanning stage with dual illumination⁷. In all instances, regardless of image dimensions, anisotropy was resolved, and isotropic structural integrity was achieved⁷ [Figs. 1(f), 3(b), 3(b')-3(b'''), and 4].

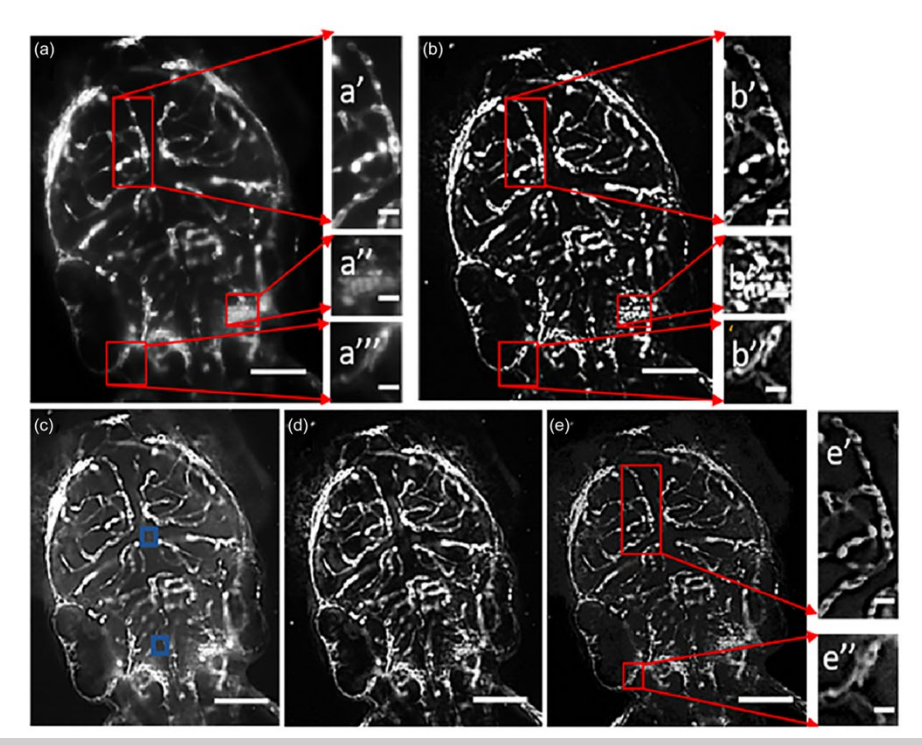


Figure 3^7 . Image processing to resolve fine details. (a) Unprocessed image. Scale bar: 200 μm. (a') Magnification of middle mesencephalic artery. (a'') Magnification of primordial hindbrain. (a''') Magnification of posterior cerebral vein. Scale bar for (a')–(a'''): 50 μm. (b) Super-resolved image. Scale bar: 200 μm. Scale bar (b')–(b'''): 50 μm. (c) Autofluorescence or tissue scattering are amplified along with the fluorescent signal after dehazing. Scale bar: 200 μm. Blue squares: local pixel patch with autofluorescence. (d) Fluorescent signal to noise ratio of zebrafish vasculature is enhanced using background substraction. Scale bar: 200 μm. (e) Fine vasculature is resolved after deconvolution of dehazed PSF. Scale bar: 200 μm. Scale bar (e') and (e''): 50 μm.

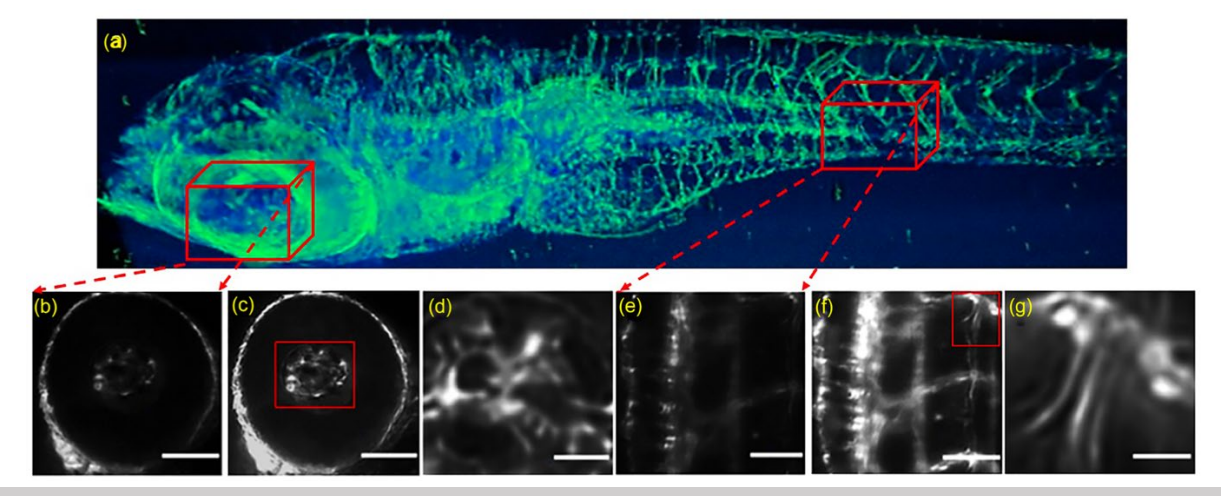


Figure 4^7 . Application of technique to super-resolution image acquired via oblique scanning method. (a) 3D reconstruction of the vasculature of a 4 days post fertilization (dpf) zebrafish. (b) High resolution image taken from the large FOV. Scale bar: $100 \ \mu m$. (c) Intensity of image (b) is corrected and edges between features are resolved through dehazing and background subtraction. Scale bar: $100 \ \mu m$. (d) Magnification of red box area from image (c) showing detail of super-resolution scanning.

Scale bar: 30 μ m. (e) High resolution image taken from the large FOV. Scale bar: 100 μ m. (f) Intensity correction and resolution of edges between features of image (e) achieved through dehazing and background subtraction. Scale bar: 100 μ m. (g) Super-resolution details from red box area in image (f). Scale bar: 30 μ m.

FEATURE DETECTION TO SEGMENT CARDIOMYOCYTES FOR INVESTIGATING CARDIAC CONTRACTILITY

Based on recovering the anisotropic fluorescent intensity, further application to in vivo zebrafish heart for biomechanical quantification. Myocardial contractility is an important factor of healthy cardiac function ¹⁷. Contractility is regulated by cardiomyocytes, which comprise a significant portion of the myocardium ¹⁸. Proper investigation of cardiomyocyte physiology and pathophysiology depends on the ability to visualize individual cardiomyocytes with respect to the surrounding tissue ¹⁹. For instance, precise counting of cardiomyocytes to understand cell proliferation during cardiogenesis ^{20,21} can only be achieved if separate and distinct cardiomyocytes are observable. Limitations of invasive histological investigation, such as small sampling size and low cell viability, make it difficult to demonstrate statistical significance ⁴. Imaging transgenic zebrafish with LSFM enables *in vivo* 4D optical sectioning for study of cardiac architecture ^{6,7,23,24}. Even so, specimen movement and sampling artifacts negatively affect focus, making it a challenge to quantify biomarker data ⁵.

On the whole, optical microscopy offers a vast spectrum of complex image attributes available for feature selection¹, which presents an obstacle in research that relies on confidence in biomarker data. With a large range of target attributes available across image datasets, manual analysis becomes impractical and unreliable^{2,3}. Feature detection methods can be employed to discard irrelevant attributes and reduce data dimensionality^{1,2}. This is useful in volumetric

reconstruction of images, which requires high sensitivity in feature detection. This applies to aberrations like tissue protrusions, illumination changes, scaling differences, and motion²⁷, which can all cause feature redundancy in images²⁶.

Manual boundary delineation of fused cardiomyocyte nuclei volumes is time-consuming because boundaries are poorly defined or entirely undiscernible⁵ [Fig. 5(a)]. Additionally, because of background fluorescence present in light sheet fluorescence microscopy⁵, poor contrast between neighboring cardiomyocytes is a pervasive issue⁷ [Figs. 6(a) and 6(d)]. Further contributing to the problem are low sampling rates, autofluorescence, and dynamic motion of the heart convoluting the lateral and axial imaging planes and interfering with optimal image quality⁵ [Figs. 5(b)-5(d)].

Intensity-based separation techniques like Otsu's method, iso data thresholding, entropy-based thresholding, and adaptive thresholding can be used for automated cell tracking, but these methods are known to perform poorly when noise is present, and consequently do not allow separation of clustered objects into distinctly individual objects²⁸. These techniques are further hindered by optical aberrations, short exposure times, movement of cells in and out of the field of view, and poor contrast between cells^{3,27}. The watershed algorithm is another popular strategy, but it is highly prone to over-segmentation, and factors like noise or complex cell morphology can result in false detection of features^{3,28}. Owing to these limitations, an alternate method is needed for separating the target biomarker from its immediate surroundings and creating distinct and meaningful biological regions.

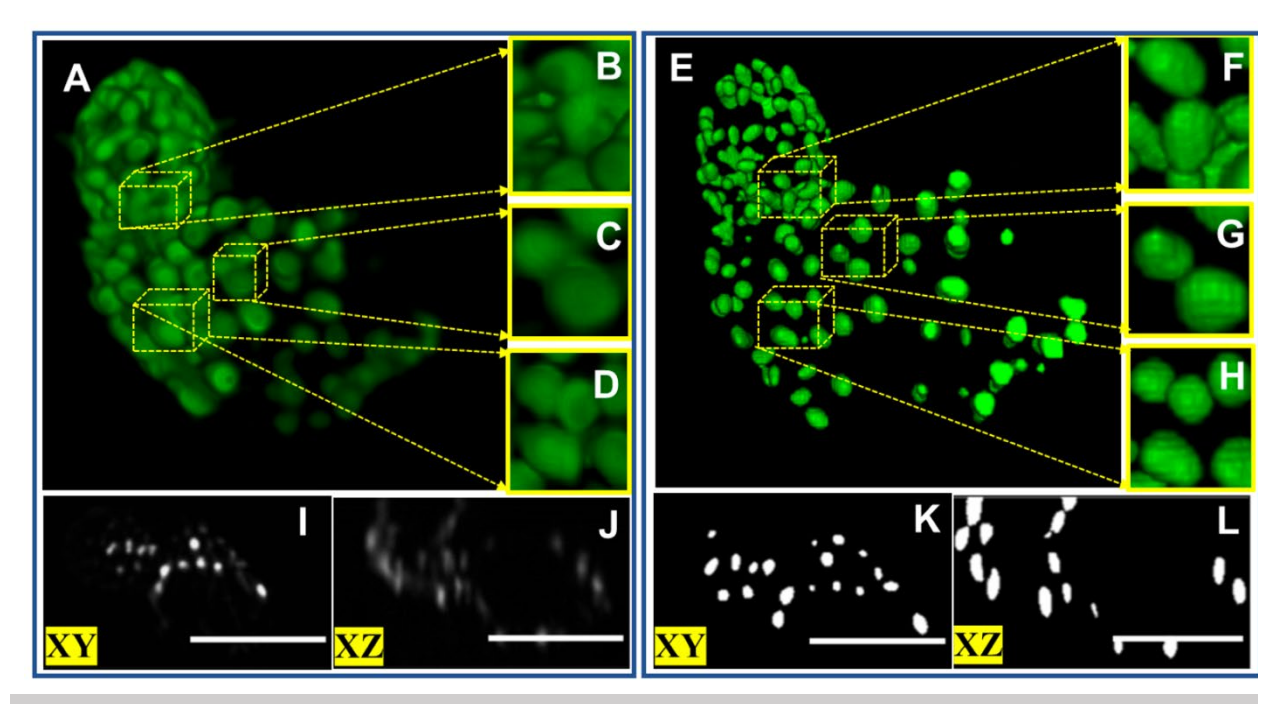


Figure 5⁵: Using Difference of Gaussian filter and watershed algorithm to individualize cardiomyocyte nuclei. (A) 2 dpf volumetric reconstruction of zebrafish cardiomyocytes, acquired using light sheet fluorescence microscopy and used to visualize time dependent motion of cardiomyocytes. (B-D) Magnifications of image (A) showing tight clusters of cardiomyocytes. Tracking and counting cardiomyocytes is hampered by density of clusters. (E) Difference of Gaussian (DoG) method is applied along with the watershed algorithm to individualize clustered cardiomyocytes. (F-H) Magnifications of image (E) demonstrating distinctness of each cardiomyocyte compared to those seen in images (B-D). (I-J) 2D lateral and axial views showing object overlap due to increased noise from complex tissue morphology. Scale bar: 50 μm. (K-L) Lateral and axial segments as binary data are used to verify curvature of the marker cardiomyocytes. Scale bar: 50 μm.

The pre-processing technique that addresses this need involves first the difference of Gaussian (DoG) scale-space bandpass operation to reduce noise and minimize false positives²⁹. Rather than relying on brightness variation to identify features as binary images, this detection technique instead focuses on sensitivity to edges through the human visual perception (HVP) model^{26,30,31}. Next, the watershed algorithm is used, yielding segmented cardiomyocytes even in a relatively dense 48 hours post fertilization (hpf) cluster of cells⁵ [Figs. 5(e)-5(h)]. Since the processed images were binary, the watershed algorithm doesn't over-segment by detecting background or autofluorescent noise.

Because the DoG method filters out high frequency noise, under-detection of features is a possiblility²⁵. In comparatively dense fields of 72 and 96 hpf cardiomyocytes, low pixel intensities produced by the DoG edge detector results in under-segmentation and incorrect cell tracking⁵ [Figs. 6(b) and 6(e)]. Such under-detection is counteracted through application of local contour detection with the Hessian matrix²². The HPV-based Hessian difference of Gaussian (HDoG) strategy locates saddle points³², which are points in a function that represent neither an intensity maximum nor minimum and can indicate merged nuclei borders⁵. allows for precise identification of cardiomyocyte nuclei boundaries and individual volumes even in dense cell environments⁵ [Figs. 6(c) and 6(f)].

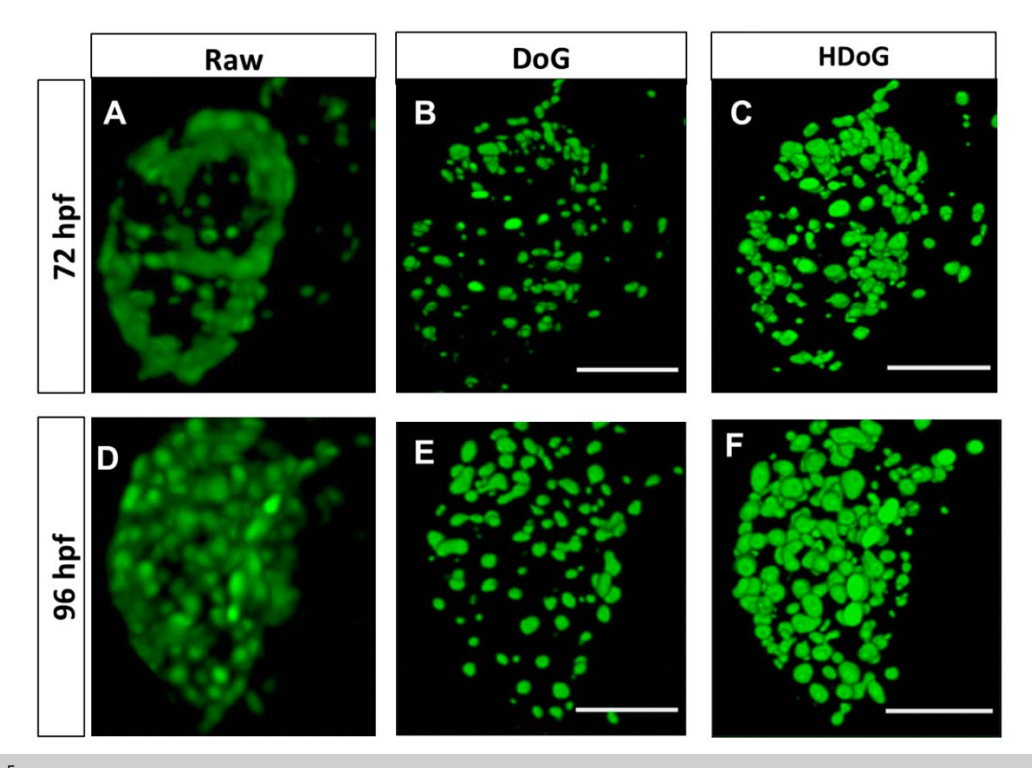


Figure 6⁵. Segmenting overlapping cardiomyocyte nuclei using the watershed algorithm and Hessian Difference of Gaussian. (A, D) Unprocessed volumetric reconstructions of (A) 3 dpf and (D) 4 dpf zebrafish cardiomyocytes. Higher density of cardiomyocytes results in more light scattering, yielding blurred images. (B, E) Watershed algorithm and Difference of Gaussian (DoG) detector applied to (B) 3 dpf and (E) 4 dpf volumes results in under segmentation and inaccurate cardiomyocyte tracking. Scale bar: 50 μm. (C, F) Watershed algorithm and Hessian Difference of Gaussian (HDoG) are applied

to the (C) 3 dpf and (F) 4 dpf cardiomyocyte volumes, resulting in more sensitive and accurate blob detection and segmentation. Scale bar: 50 µm.

This edge detection technique can be coupled with post-processing methods like top-hat and bottom-hat transform, to remove redundant binary features^{22,26}, and applied to cell studies in developmental biology^{3,34}. It has been used to identify and track cardiomyocyte nuclei, thereby allowing quantification of *in vivo* contractility in the zebrafish heart during distinct phases of development⁵. Using this technique, dynamic cardiomyocyte movement through the cardiac cycle was visualized at 48 hpf [Figs. 7(a)-7(d)], at 72 hpf [Figs. 7(e)-7(h)], and at 96 hpf [Figs. 7(i)-7(l)]. The HDoG edge detector was able to segment the cardiomyocyte nuclei regardless of anisotropic Gaussian luminance, fast frame rates required for imaging, and the increasingly dense cell environments of more mature developmental stages⁵. The HDoG edge detector can be used not only for segmenting and counting cardiomyocytes, but for any other type of cell, no matter the orientation or heterogeneity of sizes⁵.

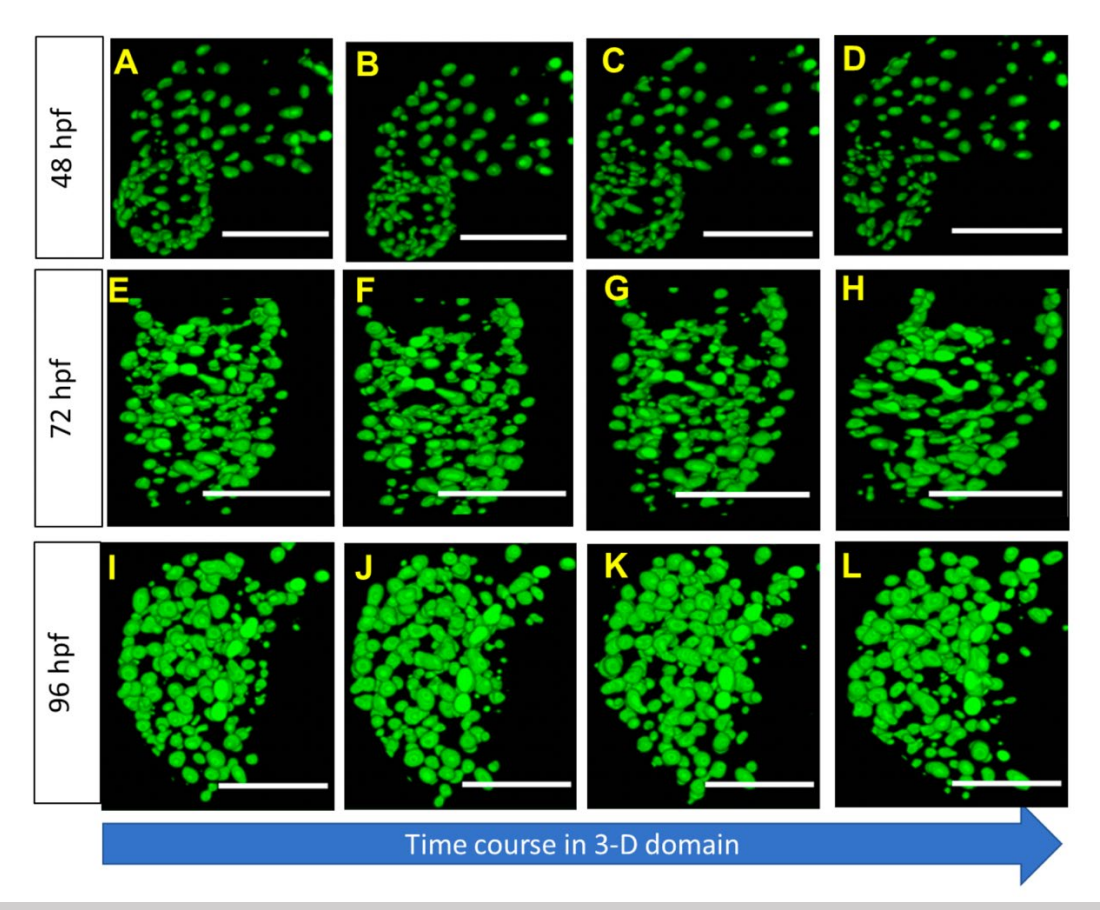


Figure 7^5 . Separating cardiomyocytes in differing tissue morphologies of multiple developmental stages. (A-D) Visualizations of dynamic 2 dpf zebrafish cardiomyocytes. Scale bar: 50 μ m. (E-H) 3 dpf dynamic cardiomyocytes individualized through use of Hessian Difference of Gaussian detector. Scale bar: 50 μ m. (I-L) 4 dpf cardiomyocytes are detected and isolated using the image processing methods, despite the fast frame rates needed to sample contractility. Scale bar: 50 μ m.

Application of this biomarker edge detection method is proving to be a useful tool in cell morphology studies, cell proliferation studies, developmental signaling mechanotransduction⁵. For instance, this method was used to demonstrate cardiac maturation through quantification of the outermost curvature having a higher area ratio than the innermost curvature⁵. Cardiomyocyte nuclei were tracked across developmental stages ranging from 48 hpf to 120 hpf [Figs. 8(a)-8(h)]. Stretch level changes in the developing zebrafish heart were investigated along with area ratio comparisons between innermost and outermost curvature areas⁵. After

analyzing the time course of area ratio using three cardiomyocytes as markers, it was found that the area ratio of the outermost curvature area the opposite side of the atrioventricular canal receiving blood pumped in from the atrium) displays a higher area ratio than the innermost curvature of the ventricle, though the area ratio for both regions increase consistently⁵ [Figs. 8(i) and 8(j)].

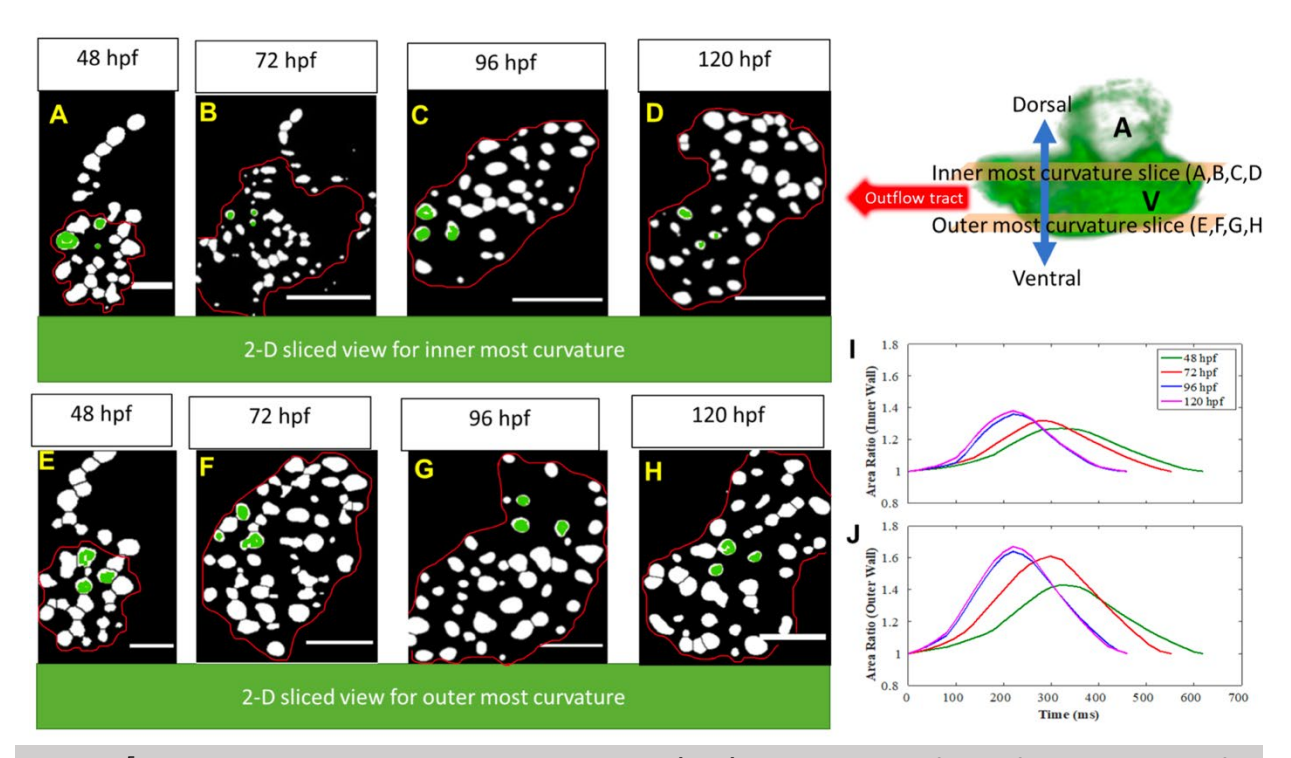


Figure 8⁵. Area ratio analysis using selected markers. (A-D) 2D slice views of zebrafish dorsal area of ventricle highlighting the innermost curvature for (A) 2 dpf, (B) 3 dpf, (C) 4 dpf, and (D) 5 dpf zebrafish. Scale bar for (A): 30 μ m. Scale bar for (B-D): 50 μ m. (E-H) 2D slices of ventral part of zebrafish heart highlighting the outermost ventricle curvature for (E) 2 dpf, (F) 3 dpf, (G) 4 dpf, and (H) 5 dpf zebrafish. Scale bar for (E): 30 μ m. Scale bar for (F-H): 50 μ m. (I) Three cardiomyocytes highlighted in (A-D) are tracked in area ratio for innermost curvature and demonstrate increasing contractility of the developing zebrafish heart. (J) Three cardiomyocytes (E-H) are tracked in area ratio of outermost curvature and show that the outermost curvature has higher contractility than the innermost curvature.

Summary

Novel image processing for LSFM adopted for biomechanical quantification would be able to solve important biological questions including developmental biology, molecular biology, and genetics in Mechanobiology manner. Specifically, dynamic sample images, such as heart or rapid cell movement as well as calcium transient of tissue, previously remained challenging problems although other image modalities have been developed. Light-sheet microscope with high-end camera has been overcome aforementioned problems, still diminishing fluorescent intensity or tissue scattering exacerbated original image qualities to biomechanical quantification or cell signaling analysis. This recently published papers will be beneficial in various research society.

References

- 1. Bolón-Canedo V, Remeseiro B. Feature selection in image analysis: a survey. *Artif Intell Rev.* 2020;53(4):2905-2931. doi:10.1007/s10462-019-09750-3
- 2. Torres R, Judson-Torres RL. Research Techniques Made Simple: Feature Selection for Biomarker Discovery. *J Invest Dermatol*. 2019;139(10):2068-2074.e1. doi:https://doi.org/10.1016/j.jid.2019.07.682
- 3. Meijering E, Dzyubachyk O, Smal I, van Cappellen WA. Tracking in cell and developmental biology. *Semin Cell Dev Biol*. 2009;20(8):894-902. doi:https://doi.org/10.1016/j.semcdb.2009.07.004
- 4. Wright PT, Tsui SF, Francis AJ, MacLeod KT, Marston SB. Approaches to High-Throughput Analysis of Cardiomyocyte Contractility. *Front Physiol.* 2020;11:612. doi:10.3389/fphys.2020.00612
- 5. Teranikar, T., Villarreal, C., Salehin, N., Lim, J., Ijaseun, T., Cao, H., . . . Lee, J. (2021). Feature Detection to Segment Cardiomyocyte Nuclei for Investigating Cardiac Contractility. bioRxiv, 2021.2003.2003.433810. https://doi.org/10.1101/2021.03.03.433810
- 6. Olarte, O. E., Andilla, J., Gualda, E. J., & Loza-Alvarez, P. (2018). Light-sheet microscopy: a tutorial. Advances in Optics and Photonics, 10(1), 111-179. https://doi.org/10.1364/AOP.10.000111
- 7. Teranikar, T., Messerschmidt, V., Lim, J., Bailey, Z., Chiao, J.-C., Cao, H., . . . Lee, J. (2020). Correcting anisotropic intensity in light sheet images using dehazing and image morphology. APL Bioengineering, 4(3), 036103. https://doi.org/10.1063/1.5144613
- 8. Johnsen, S. (2014). Hide and Seek in the Open Sea: Pelagic Camouflage and Visual Countermeasures. Annual Review of Marine Science, 6(1), 369-392. https://doi.org/10.1146/annurev-marine-010213-135018
- 9. Jing, D., Zhang, S., Luo, W., Gao, X., Men, Y., Ma, C., . . . Zhao, H. (2018). Tissue clearing of both hard and soft tissue organs with the PEGASOS method. Cell Research, 28(8), 803-818. https://doi.org/10.1038/s41422-018-0049-z
- 10. Crosignani, V., Dvornikov, A., Aguilar, J., Stringari, C., Edwards, R., Mantulin, W., & Gratton, E. (2012). Deep tissue fluorescence imaging and in vivo biological applications. Journal of Biomedical Optics, 17(11), 116023.
- 11. Bagge, L. E., Kinsey, S. T., Gladman, J., & Johnsen, S. (2017). Transparent anemone shrimp (Ancylomenes pedersoni) become opaque after exercise and physiological stress in correlation with increased hemolymph perfusion. Journal of Experimental Biology, 220(22), 4225-4233. https://doi.org/10.1242/jeb.162362
- 12. Žuži M, Čejka J, Bruno F, Skarlatos D and Liarokapis F (2018) Impact of Dehazing on Underwater Marker Detection for Augmented Reality. Front. Robot. AI 5:92. doi: 10.3389/frobt.2018.00092M. A. Malathi V, Int. J. Eng. Adv. Technol. (IJEAT) 9(2), 280 (2019).
- 13. Lu, H., Li, Y., Zhang, L., & Serikawa, S. (2015). Contrast enhancement for images in turbid water. Journal of the Optical Society of America A, 32(5), 886-893. https://doi.org/10.1364/JOSAA.32.000886
- 14. T. M. Nimisha, K. Seemakurthy, A. N. Rajagopalan, N. Vedachalam, and, and R. Raju, in Proceedings of the Tenth Indian Conference on Computer Vision, Graphics and Image

- Processing (Association for Computing Machinery, Guwahati, Assam, 2016), Article No. 26.
- 15. He, K., Sun, J., & Tang, X. (2011). Single Image Haze Removal Using Dark Channel Prior. IEEE Transactions on Pattern Analysis and Machine Intelligence, 33(12), 2341-2353. https://doi.org/10.1109/TPAMI.2010.168
- 16. Nollet EE, Manders EM, Goebel M, Jansen V, Brockmann C, Osinga J, van der Velden J, Helmes M and Kuster DWD (2020) Large-Scale Contractility Measurements Reveal Large Atrioventricular and Subtle Interventricular Differences in Cultured Unloaded Rat Cardiomyocytes. Front. Physiol. 11:815. doi: 10.3389/fphys.2020.00815
- 17. Morrissy, S., & Chen, Q. M. (2010, July 12). Oxidative stress and heart failure. Comprehensive Toxicology (Second Edition). Retrieved from https://www.sciencedirect.com/science/article/pii/B9780080468846007119
- 18. Legrice I, Pope A, Smaill B. The Architecture of the Heart: Myocyte Organization and the Cardiac Extracellular Matrix. In: Vol 253.; 2005:3-21. doi:10.1007/0-387-22825-X 1
- 19. de Pater E, Clijsters L, Marques SR, et al. Distinct phases of cardiomyocyte differentiation regulate growth of the zebrafish heart. *Development*. 2009;136(10):1633 LP 1641. doi:10.1242/dev.030924
- 20. Bensley JG, De Matteo R, Harding R, Black MJ. Three-dimensional direct measurement of cardiomyocyte volume, nuclearity, and ploidy in thick histological sections. *Sci Rep.* 2016;6(1):23756. doi:10.1038/srep23756
- 21. Fei P, Lee J, Packard RR, et al. Cardiac Light-Sheet Fluorescent Microscopy for Multi-Scale and Rapid Imaging of Architecture and Function. *Sci Rep.* 2016;6:22489. doi:10.1038/srep22489
- 22. Beucher S, Mathmatique C. The Watershed Transformation Applied To Image Segmentation. *Scanning Microsc.* 2000;6.
- 23. Bakkers J. Zebrafish as a model to study cardiac development and human cardiac disease. *Cardiovasc Res.* 2011;91(2):279-288. doi:10.1093/cvr/cvr098
- 24. Major, R. J., & Poss, K. D. (2007). Zebrafish Heart Regeneration as a Model for Cardiac Tissue Repair. Drug discovery today. Disease models, 4(4), 219–225. https://doi.org/10.1016/j.ddmod.2007.09.002
- 25. Yin X, Ng BW-H, He J, Zhang Y, Abbott D. Accurate Image Analysis of the Retina Using Hessian Matrix and Binarisation of Thresholded Entropy with Application of Texture Mapping. *PLoS One*. 2014;9(4):1-17. doi:10.1371/journal.pone.0095943
- 26. El-gayar MM, Soliman H, meky N. A comparative study of image low level feature extraction algorithms. *Egypt Informatics J.* 2013;14(2):175-181. doi:https://doi.org/10.1016/j.eij.2013.06.003
- 27. Xu Y, Wu T, Gao F, Charlton JR, Bennett KM. Improved small blob detection in 3D images using jointly constrained deep learning and Hessian analysis. *Sci Rep.* 2020;10(1):326. doi:10.1038/s41598-019-57223-y
- 28. Bharodiya AK, Gonsai AM. An improved edge detection algorithm for X-Ray images based on the statistical range. *Heliyon*. 2019;5(10):e02743-e02743. doi:10.1016/j.heliyon.2019.e02743
- 29. Zhang, H., Li, Y., Chen, H., Yuan, D., & Sun, M. (2013). Perceptual Contrast Enhancement with Dynamic Range Adjustment. Optik, 124(23), 10.1016/j.ijleo.2013.04.046. https://doi.org/10.1016/j.ijleo.2013.04.046

- 30. So S, Johnsen S. Lifting the Cloak of Invisibility: The Effects of Changing Optical Conditions on Pelagic Crypsis 1. Vol 43.; 2003.
- 31. Kulikov V, Guo S-M, Stone M, et al. DoGNet: A deep architecture for synapse detection in multiplexed fluorescence images. *PLOS Comput Biol.* 2019;15(5):1-20. doi:10.1371/journal.pcbi.1007012
- 32. Marsh BP, Chada N, Sanganna Gari RR, Sigdel KP, King GM. The Hessian Blob Algorithm: Precise Particle Detection in Atomic Force Microscopy Imagery. Sci Rep. 2018;8(1):978. doi:10.1038/s41598-018-19379-x